ARTICLE IN PRESS

Computers and Mathematics with Applications ▮ (▮▮▮▮) ▮▮▮–▮▮▮

Contents lists available at SciVerse ScienceDirect

Computers and Mathematics with Applications

journal homepage: www.elsevier.com/locate/camwa

Spectral-element discontinuous Galerkin lattice Boltzmann simulation of flow past two cylinders in tandem with an exponential time integrator

Kalu Chibueze Uga [a], Misun Min [b], Taehun Lee [a,*], Paul F. Fischer [b]

[a] Department of Mechanical Engineering, City College of City University of New York, New York, NY 10031, USA
[b] Mathematics and Computer Science Division, Argonne National Laboratory, Argonne, IL 60439, USA

ARTICLE INFO

Keywords:
Lattice Boltzmann method
Exponential integrator
Spectral element
Discontinuous Galerkin
Tandem cylinders

ABSTRACT

In this paper, a spectral-element discontinuous Galerkin (SEDG) lattice Boltzmann discretization and an exponential time-marching scheme are used to study the flow field past two circular cylinders in tandem arrangement. The basic idea is to discretize the streaming step of the lattice Boltzmann equation by using the SEDG method to get a system of ordinary differential equations (ODEs) whose exact solutions are expressed by using a large matrix exponential. The approximate solution of the resulting ODEs are obtained from a projection method based on a Krylov subspace approximation. This approach allows us to approximate the matrix exponential of a very large and sparse matrix by using a matrix of much smaller dimension. The exponential time integration scheme is useful especially when computations are carried out at high Courant–Friedrichs–Lewy (*CFL*) numbers, where most explicit time-marching schemes are inaccurate. Simulations of flow were carried out for a circular cylinder at $Re = 20$ and for two circular cylinders in tandem at $Re = 40$ and a spacing of $2.5D$, where D is the diameter of the cylinders. We compare our results with those from a fourth-order Runge–Kutta scheme that is restricted by the *CFL* number. In addition, important flow parameters such as the drag coefficients of the two cylinders and the wake length behind the rear cylinder were calculated by using the exponential time integration scheme. These results are compared with results from our simulation using the RK scheme and with existing benchmark results.

© 2012 Elsevier Ltd. All rights reserved.

1. Introduction

In this paper, we present an exponential time integration scheme for solving the semidiscrete spectral-element discontinuous Galerkin lattice Boltzmann equation (LBE), resulting from the spatial discretization of partial differential equations of the hyperbolic type [1], for flow past two circular cylinders in tandem.

The exponential time integrator is a high-order time-marching scheme [2] that gives a good approximation to the resulting n system of ordinary differential equations (ODEs) yielding a large matrix $A \in R^{n\times n}$ with n unknowns. Consider a one-dimensional ODE of the form $\frac{df}{dt} + cf = 0$, where f is the unknown and c a constant. The exact solution is given as $f = f(0)e^{-ct}$, with an initial condition $f(0)$. For this solution the exponential can be easily computed. For the cases where the constant is a large matrix, A, however, we need to seek an alternate approach to evaluate the matrix exponential. Our exponential time integration scheme approximates the exponential of the larger matrix A by using a small matrix, H, known as the Hessenberg matrix. The matrix H is obtained from the Krylov subspace whose elements are computed by the Arnoldi

* Corresponding author.
E-mail addresses: kuga00@ccny.cuny.edu (K.C. Uga), mmin@mcs.anl.gov (M. Min), thlee@ccny.cuny.edu (T. Lee), fischer@mcs.anl.gov (P.F. Fischer).

0898-1221/$ – see front matter © 2012 Elsevier Ltd. All rights reserved.
doi:10.1016/j.camwa.2011.12.059

Please cite this article in press as: K.C. Uga, et al., Spectral-element discontinuous Galerkin lattice Boltzmann simulation of flow past two cylinders in tandem with an exponential time integrator, Computers and Mathematics with Applications (2012), doi:10.1016/j.camwa.2011.12.059

algorithm [3]. The accuracy in approximating the matrix exponential depends on several factors, including the accuracy of the polynomial approximation of the Arnoldi vectors and the order of the Krylov subspace [4]. One can choose the order of the Krylov subspace so that it is small enough to compute efficiently and still give an accurate enough solution of the matrix exponential.

Over the years, several studies have been done on the flow past an isolated circular cylinder and cylinders in either tandem or staggered arrangements. These studies have been motivated by the practical importance of such cylinders in engineering applications and on the increasing use of cylindrical geometry in industrial applications. This geometry often forms the basic structure found in heat exchangers and in the columns of bridges where the cylindrical configurations are exposed to fluid in motion. Knowing the motion of the fluid in the vicinity of the cylinders is of practical importance because the safety and longevity of these structures are important. Also, knowledge of the flow in relation to the arrangement of the cylinders is important especially in understanding the vibration of bridge columns. This includes how each cylinder affects its neighbor and the overall flow within the region under consideration.

The incompressible flow over an isolated cylinder has been studied by many researchers [1,5–8]. The results already published provide a good benchmark case to validate new numerical schemes. Extension to two cylinders with different spacing between them becomes more challenging, especially when the Reynolds number Re is high and vortex shedding is observed. The wake between the cylinders in tandem arrangement behaves differently depending on the spacing between the centers of the cylinder. Moreover, the wake behind cylinders in tandem arrangement is different from the wake behind an isolated cylinder because of the flow features caused by the presence of the second cylinder [9]. Also, beyond a critical spacing between the cylinders, it has been observed that two vortex streets are generated, one for each cylinder, behind the rear cylinder. For spacings less than the critical spacing, the vortex street from the first cylinder reattaches to the surface of the second cylinder so that only one vortex street is seen beyond the rear cylinder [10–12].

Singha and Sinhamahapatra [12] used the Navier–Stokes (NS) equations with a second-order, implicit finite-volume method to study the low Reynolds number incompressible flow about two cylinders in tandem. In their work, the spacing between the centers of the cylinders was varied and analyzed individually for different Reynolds number. Sharman et al. [10] studied the flow over two tandem cylinders at $Re = 100$ using an unstructured NS solver. Their results showed that even for this value of Re, the flow is still laminar. Also, their results showed that the critical spacing (spacing beyond which two vortex streets are seen behind the rear cylinder) between the centers of the cylinders for this Reynolds number is between $3.75D$ and $4.00D$, where D is the diameter of the cylinders. Mussa et al. [11] performed studies similar to those in [10] by using a multiple relaxation time (MRT) LBM and showed that the critical spacing between the centers of the cylinders for $Re = 100$ is between $3.25D$ and $3.50D$; they pointed out that the discrepancy is due to the multiplicity of stable solutions in the region between the cylinders.

For this study, simulations were carried out in a rectangular domain with Reynolds numbers at 20 and 40 for an isolated cylinder and cylinders in tandem arrangement, respectively. For a constant Courant–Friedrichs–Lewy (CFL) number, we investigated the effect of varying the order of quadrilateral element, N, and the order of the Krylov subspace, m. Quantities measured were the drag coefficient on the front and rear cylinders, and the wake length generated behind the rear cylinder. Computations that involve higher N and m usually take longer to complete because of the increased number of the Gauss–Lobatto–Legendre points [13] on each quadrilateral element and the increased order of Krylov subspace. We carried out simulations of low Reynolds number flow over a circular cylinder to validate our code. Quantitative results from numerical experiments were compared with results from the literature to ensure that our method is valid.

This paper is organized as follows. In Section 2, we discuss a spectral-element discontinuous Galerkin lattice Boltzmann discretization. In Section 3, we discuss the exponential time integration method for solving the semidiscrete spectral-element discontinuous Galerkin lattice Boltzmann equation. In Section 4, we present the computational results. In Section 5, we summarize our conclusions.

2. SEDG-LBM

The spectral-element discontinuous Galerkin lattice Boltzmann method (SEDG-LBM) [1] is local in space and can be applied to complex geometries due to the grid structure. The solutions are discontinuous on the nodes along the faces of the elements that are shared. Also, the mass matrix is fully diagonal and can be easily inverted.

2.1. Lattice Boltzmann equation

We consider the discrete Boltzmann equation with the Bhatnagar–Gross–Krook collision operator [14],

$$\frac{\partial f_\alpha}{\partial t} + \mathbf{e}_\alpha \cdot \nabla f_\alpha = -\frac{f_\alpha - f_\alpha^{eq}}{\lambda} \quad \text{on } \Omega \text{ for } \alpha = 0, 1, \ldots, N_\alpha, \tag{1}$$

where f_α is the particle distribution function defined in the direction of the microscopic particle velocity $\mathbf{e}_\alpha$, λ is the relaxation time, and N_α is the number of microscopic velocity, which depends on the lattice Boltzmann model used [15,16]. In this work, we have used a two dimensional 9-velocity model on a square lattice.

Please cite this article in press as: K.C. Uga, et al., Spectral-element discontinuous Galerkin lattice Boltzmann simulation of flow past two cylinders in tandem with an exponential time integrator, Computers and Mathematics with Applications (2012), doi:10.1016/j.camwa.2011.12.059

The discrete velocity $\mathbf{e}_\alpha$ is expressed as $\mathbf{e}_\alpha = (0,0)$ for $\alpha = 0$, $\mathbf{e}_\alpha = (\cos\theta_\alpha, \sin\theta_\alpha)$ for $\alpha = 1,2,3,4$, and $\mathbf{e}_\alpha = \sqrt{2}(\cos\theta_\alpha, \sin\theta_\alpha)$ for $\alpha = 5,6,7,8$, where $\theta_\alpha = (\alpha-1)\pi/4$. The local equilibrium distribution function is given by

$$f_\alpha^{eq} = w_\alpha \rho \left[1 + \frac{\mathbf{e}_\alpha \cdot \mathbf{u}}{c_s^2} + \frac{(\mathbf{e}_\alpha \cdot \mathbf{u})^2}{2c_s^4} - \frac{(\mathbf{u}\cdot\mathbf{u})}{2c_s^2}\right], \tag{2}$$

where w_α is the weight, ρ the density, $\mathbf{u}$ the macroscopic velocity, and c_s the speed of sound [17] given as $c_s = 1/\sqrt{3}$.

The LBE along the characteristics for time step δt is derived from the DBE in Eq. (1) as

$$f_\alpha(\mathbf{x},t) - f_\alpha(\mathbf{x} - \mathbf{e}_\alpha \delta t, t - \delta t) = -\int_{t-\delta t}^{t} \frac{f_\alpha - f_\alpha^{eq}}{\lambda} dt'. \tag{3}$$

Approximating the right-hand side of Eq. (3) with a second-order trapezoidal rule gives

$$f_\alpha(\mathbf{x},t) - f_\alpha(\mathbf{x} - \mathbf{e}_\alpha \delta t, t - \delta t) = -\frac{\delta t}{2}\left[\left.\frac{f_\alpha - f_\alpha^{eq}}{\lambda}\right|_{(\mathbf{x}-\mathbf{e}_\alpha\delta t, t-\delta t)} + \left.\frac{f_\alpha - f_\alpha^{eq}}{\lambda}\right|_{(\mathbf{x},t)}\right], \tag{4}$$

and introducing a modified particle distribution function, $\bar{f}_\alpha$, and its corresponding equilibrium distribution function, $\bar{f}_\alpha^{eq}$ [18], we have

$$\bar{f}_\alpha = f_\alpha + \frac{f_\alpha - f_\alpha^{eq}}{2\tau} \quad \text{and} \quad \bar{f}_\alpha^{eq} = f_\alpha^{eq} \tag{5}$$

where τ is the non-dimensional relaxation time given as $\lambda/\delta t$. The density and momentum can be computed by taking the zeroth and first moments, respectively:

$$\rho = \sum_{\alpha=0}^{N_\alpha} f_\alpha = \sum_{\alpha=0}^{N_\alpha} \bar{f}_\alpha, \quad \text{and} \quad \rho\mathbf{u} = \sum_{\alpha=0}^{N_\alpha} \mathbf{e}_\alpha f_\alpha = \sum_{\alpha=0}^{N_\alpha} \mathbf{e}_\alpha \bar{f}_\alpha. \tag{6}$$

Thus, in terms of the modified particle distribution function, Eq. (3) can be written as

$$\bar{f}_\alpha(\mathbf{x},t) - \bar{f}_\alpha(\mathbf{x} - \mathbf{e}_\alpha\delta t, t - \delta t) = -\frac{1}{\tau + 0.5}\left.\left(\bar{f}_\alpha - \bar{f}_\alpha^{eq}\right)\right|_{(\mathbf{x}-\mathbf{e}_\alpha\delta t, t-\delta t)}. \tag{7}$$

Eq. (7) is solved by first solving the collision step followed by the streaming step.

- Collision:

$$\bar{f}_\alpha(\mathbf{x} - \mathbf{e}_\alpha\delta t, t - \delta t) := \bar{f}_\alpha(\mathbf{x} - \mathbf{e}_\alpha\delta t, t - \delta t) - \frac{1}{\tau + 0.5}\left.\left(\bar{f}_\alpha - \bar{f}_\alpha^{eq}\right)\right|_{(\mathbf{x}-\mathbf{e}_\alpha\delta t, t-\delta t)}. \tag{8}$$

- Streaming:

$$\bar{f}_\alpha(\mathbf{x},t) = \bar{f}_\alpha(\mathbf{x} - \mathbf{e}_\alpha\delta t, t - \delta t). \tag{9}$$

In the classical Lattice Boltzmann finite difference approach where a structured grid is used, the grid points coincide with the lattice points so that the streaming step, as seen in Eq. (9), is a perfect shift. For this case, the *CFL* number based on $\mathbf{e}_\alpha$ is unity. Whereas, on unstructured grids, the streaming step is either interpolated or solved by expressing it as a solution of the advection equation:

$$\frac{\partial \bar{f}_\alpha}{\partial t} + \mathbf{e}_\alpha \cdot \nabla \bar{f}_\alpha = 0. \tag{10}$$

The accuracy of the method used to solve Eq. (10) depends on the order of accuracy of the scheme used. In the following subsection, we discuss how the SEDG approach is used to discretize the advection equation.

2.2. SEDG weak formulation

To solve the advection equation in Eq. (10), we consider our computational domain Λ, consisting of nonoverlapping elements Λ^e, such that $\Lambda = \cup_{e=1}^{E} \Lambda^e$, and we define a flux $\mathbf{F}_\alpha(\bar{f}) = \mathbf{e}_\alpha \bar{f}_\alpha$ for the velocity vector $\mathbf{e}_\alpha = (e_{\alpha x}, e_{\alpha y})$. Thus on Λ, Eq. (10) can be written as in [1]

$$\frac{\partial \bar{f}_\alpha}{\partial t} + \nabla \cdot \mathbf{F}_\alpha(\bar{f}) = 0. \tag{11}$$

With a local test function ϕ multiplied on the advection equation, we have

$$\left(\frac{\partial \bar{f}_\alpha}{\partial t} + \nabla \cdot \mathbf{F}_\alpha(\bar{f}), \phi\right)_{\Lambda^e} = 0. \tag{12}$$

Please cite this article in press as: K.C. Uga, et al., Spectral-element discontinuous Galerkin lattice Boltzmann simulation of flow past two cylinders in tandem with an exponential time integrator, Computers and Mathematics with Applications (2012), doi:10.1016/j.camwa.2011.12.059

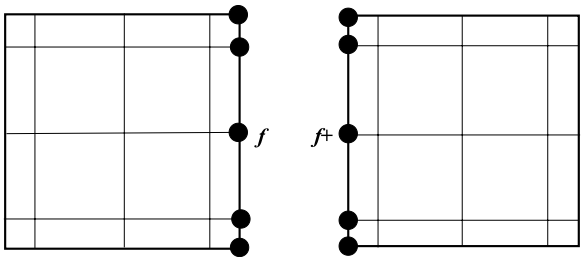

Fig. 1. $\mathbf{F}^*$ as a function of $\bar{f}$ and $\bar{f}^+$.

Integrating Eq. (12) by parts, we get

$$\int_{\Lambda^e} \phi \frac{\partial \bar{f}_\alpha}{\partial t} d\Lambda - \int_{\Lambda^e} \mathbf{F}_\alpha(\bar{f}) \cdot \nabla \phi d\Lambda = -\int_{\partial \Lambda^e} \phi \mathbf{n} \cdot \mathbf{F}_\alpha(\bar{f}) d\bar{\Lambda}, \tag{13}$$

where $\bar{\Lambda}$ represents the surface boundary of the element Λ^e and $\mathbf{n} = (n_x, n_y)$ is the unit normal vector pointing outward. We introduce a numerical flux $\mathbf{F}^*$, which is a function of the local solution $\bar{f}$ and the neighboring solution $\bar{f}^+$ at the interfaces between neighboring elements as shown in Fig. 1. The numerical flux combines the two solutions that are allowed to be different at the neighboring element interfaces. The analytic flux $\mathbf{F}_\alpha(\bar{f})$, on the surface boundary, is replaced by the numerical flux $\mathbf{F}^*_\alpha(\bar{f})$ so that Eq. (13) becomes

$$\int_{\Lambda^e} \phi \frac{\partial \bar{f}_\alpha}{\partial t} d\Lambda - \int_{\Lambda^e} \mathbf{F}_\alpha(\bar{f}) \cdot \nabla \phi d\Lambda = -\int_{\partial \Lambda^e} \phi \mathbf{n} \cdot \mathbf{F}^*_\alpha(\bar{f}) d\bar{\Lambda}. \tag{14}$$

Integrating Eq. (14) by parts, we obtain the final form of the weak formulation as follows:

$$\left(\frac{\partial \bar{f}_\alpha}{\partial t} + \nabla \cdot \mathbf{F}_\alpha(\bar{f}), \phi \right)_{\Lambda^e} = \left(\mathbf{n} \cdot \left[\mathbf{F}_\alpha(\bar{f}) - \mathbf{F}^*_\alpha(\bar{f}) \right], \phi \right)_{\partial \Lambda^e}. \tag{15}$$

In our simulation, we use the Lax–Friedrichs flux [1,19–21] for the numerical flux $\mathbf{F}^*_\alpha(\bar{f}) = \mathbf{F}^*_\alpha(\bar{f}, \bar{f}^+)$ [1].

2.3. SEDG discretization

We consider the ordered set of $N+1$ Gauss–Lobatto–Legendre (GLL) quadrature nodes $\{\xi_0, \xi_1, \ldots, \xi_N\}$ that are the solutions of the equation

$$(1-\xi^2) L'_N(\xi) = 0, \quad \xi \in [-1, 1], \tag{16}$$

where $L'_N(\xi)$ is the derivative of the Nth-order Legendre polynomial $L_N(\xi)$. The one-dimensional Lagrange interpolation basis with the GLL grids [13,22] is given by

$$l_i(\xi) = \frac{-1}{N(N+1)} \frac{(1-\xi^2) L_N{}'(\xi)}{(\xi - \xi_i) L_N(\xi_i)}, \quad 0 \le i \le N, \ \xi \in [-1, 1]. \tag{17}$$

Now we consider our computational domain Λ in two-dimensional space. Each $(x, y) \in \Lambda^e$ is mapped on the reference domain, $(\xi, \eta) \in I = [-1, 1]^2$, through the Gordon–Hall mapping [13]. The tensor-product structure of the reference element I allows us to define a two-dimensional basis as $\psi_{ij}(\xi, \eta) = l_i(\xi(x)) l_j(\eta(y))$, or simply ψ_{ij}.

We seek a local approximate solution in Λ^e defined by the finite expansion of the tensor product basis $\psi_{ij}(\xi, \eta)$ as

$$\bar{f}^N_\alpha := \bar{f}^N_\alpha(x, y, t) = \sum_{i,j=0}^{N} (\bar{f}^N_\alpha)_{ij} \psi_{ij}(\xi, \eta), \tag{18}$$

where $(\bar{f}^N_\alpha)_{ij} = \bar{f}^N_\alpha(x_i, y_j, t)$, that is, the nodal values of the approximate solution $\bar{f}^N_\alpha$ at time t on the tensor product of the one-dimensional GLL quadrature nodes, (ξ_i, η_j) [13].

Substituting $\bar{f}^N_\alpha$ into Eq. (15) and using a test function chosen from the tensor product basis, namely, $\phi := \psi_{\tilde{i}\tilde{j}}$, we have our discretized weak form as follows:

$$\frac{d(\bar{f}^N_\alpha)_{ij}}{dt} (\psi_{ij}, \psi_{\tilde{i}\tilde{j}})_{\Lambda^e} + e_{\alpha x} (\bar{f}^N_\alpha)_{ij} \left(\frac{\partial \psi_{ij}}{\partial x}, \psi_{\tilde{i}\tilde{j}} \right)_{\Lambda^e} \tag{19}$$

$$+ e_{\alpha y} (\bar{f}^N_\alpha)_{ij} \left(\frac{\partial \psi_{ij}}{\partial y}, \psi_{\tilde{i}\tilde{j}} \right)_{\Lambda^e} = \left(\mathbf{n} \cdot \left[\mathbf{F}(\bar{f}^N_\alpha)_{ij} - \mathbf{F}^*(\bar{f}^N_\alpha)_{ij} \right], \psi_{\tilde{i}\tilde{j}} \right)_{\partial \Lambda^e}. \tag{20}$$

Please cite this article in press as: K.C. Uga, et al., Spectral-element discontinuous Galerkin lattice Boltzmann simulation of flow past two cylinders in tandem with an exponential time integrator, Computers and Mathematics with Applications (2012), doi:10.1016/j.camwa.2011.12.059

Applying the Gauss quadrature rule to Eq. (19), we obtain the mass and stiffness matrices in two dimensions. For the mass matrix, we have

$$\mathbf{M} = (\psi_{ij}, \psi_{\tilde{i}\tilde{j}})_{\Lambda^e} = \sum_{k=0}^{N}\sum_{m=0}^{N} J_{km} w_k w_m l_i(\xi_k) l_i(\xi_k) l_j(\eta_m) l_j(\eta_m)$$
$$= J(\hat{M} \otimes \hat{M}), \tag{21}$$

where $J = [J_{km}]$ represents the Jacobian at each node in a local element. Note that we have

$$\hat{M}_{ij} = \sum_{k=0}^{N} w_k l_i(\xi_k) l_{\tilde{i}}(\xi_k) = \mathrm{diag}(w_i), \tag{22}$$

where $l_i(\xi_k) = 0$ for $i \neq k$ and $l_i(\xi_k) = 1$ for $i = k$. The one-dimensional mass matrix $\hat{M}$ is diagonal, and its tensor product form is also a complete diagonal matrix in two dimensions. The stiffness matrices are defined as

$$\mathbf{D}_x = \left(\frac{\partial \psi_{ij}}{\partial x}, \psi_{\tilde{i}\tilde{j}}\right) \quad \text{and} \quad \mathbf{D}_y = \left(\frac{\partial \psi_{ij}}{\partial y}, \psi_{\tilde{i}\tilde{j}}\right). \tag{23}$$

The surface integration in Eq. (20) is the one-dimensional integration on each face of the local element:

$$\mathbf{R}(\bar{f}_\alpha^N) = \sum_{s=1}^{4}\sum_{k=0}^{N} \mathcal{R}_k^s\{(\mathbf{n}\cdot\mathbf{e}_\alpha)[(\bar{f}_\alpha^N)_{ij} - (\bar{f}_\alpha^N)_{ij}^+]\} w_k J_k^s, \tag{24}$$

where $R_k^s\{\cdot\}$ extracts the information of $\{\cdot\}$ at the nodes situated on each face of the local element for the face number s. Here, $\mathbf{n}$ is the unit normal vector, and J_k^s is the surface Jacobian at the nodes on each face.

The semidiscrete scheme for Eq. (15) in a local domain Λ^e can be written in matrix form as

$$\frac{d\mathbf{f}_\alpha}{dt} + \mathbf{M}^{-1}\mathbf{D}\mathbf{f}_\alpha = \mathbf{M}^{-1}\mathbf{R}\mathbf{f}_\alpha, \tag{25}$$

where $\mathbf{f}_\alpha = [\bar{f}_\alpha^N]_{ij}$ is a solution vector, $\mathbf{D} = e_{\alpha x}\mathbf{D}_x + e_{\alpha y}\mathbf{D}_y$, and $\mathbf{R}$ is the surface integration acting on the boundary nodes on each face of the local element. A detailed description on the SEDG-LBM with the fourth-order Runge–Kutta timestepping scheme and the computational cost and efficiency of the method can be found in [1,23].

3. Exponential time integrator

Eq. (25) is a system of n ordinary differential equations with n being the number of unknowns. The equation can be written as

$$\frac{d\mathbf{f}_\alpha(t)}{dt} = -\hat{A}\mathbf{f}_\alpha(t), \tag{26}$$

where $\hat{A} = (\mathbf{M}^{-1}\mathbf{D} - \mathbf{M}^{-1}\mathbf{R})$, $\mathbf{f}_\alpha(t) = (f_{\alpha 1}, f_{\alpha 2}, \ldots, f_{\alpha n})^T$ is a vector and A is a time-independent matrix of $n \times n$. The exact solution of Eq. (26) can be obtained as

$$\mathbf{f}_\alpha(t) = e^{-\hat{A}t}\mathbf{f}_\alpha(0). \tag{27}$$

Then, the solution for the time range $[\bar{n}\delta t, (\bar{n}+1)\delta t]$ is given in the form

$$\mathbf{f}_\alpha\left((\bar{n}+1)\delta t\right) = e^{-\delta t\hat{A}}\mathbf{f}_\alpha\left(\bar{n}\delta t\right). \tag{28}$$

Denoting $\mathbf{f}_\alpha(\bar{n}\delta t)$ as $f_\alpha^{\bar{n}}$ and $\mathbf{f}_\alpha(0)$ as f_α^0, the explicit one-step method in Eq. (28) can be expressed as the computation of matrix functions of the type

$$f_\alpha^{\bar{n}} = e^{-\delta t\hat{A}} f_\alpha^0. \tag{29}$$

The Krylov subspace projection technique is aimed at appropriately projecting the exponential matrix $e^{-\delta t\hat{A}}$, which is typically very large, onto a small Krylov subspace and accurately carrying out the resulting small exponential matrix computation. In approximating $e^{-\delta t\hat{A}}$, a polynomial of order $m-1$ is used so that the matrix exponential can be expressed in terms of that polynomial. The Taylor series expansion of the exponential term in (29) is

$$e^{-\delta t\hat{A}} f_\alpha^0 = f_\alpha^0 + (-\delta t\hat{A}) f_\alpha^0 + \frac{(-\delta t\hat{A})^2}{2!} f_\alpha^0 + \frac{(-\delta t\hat{A})^3}{3!} f_\alpha^0 + \cdots. \tag{30}$$

Please cite this article in press as: K.C. Uga, et al., Spectral-element discontinuous Galerkin lattice Boltzmann simulation of flow past two cylinders in tandem with an exponential time integrator, Computers and Mathematics with Applications (2012), doi:10.1016/j.camwa.2011.12.059

The series can be truncated at order $m-1$ with a given integer m, yielding a polynomial approximation of degree $m-1$,

$$a_0 f_\alpha^0 + a_1(-\delta t\hat{A})f_\alpha^0 + a_2(-\delta t\hat{A})^2 f_\alpha^0 + \cdots + a_{m-1}(-\delta t\hat{A})^{m-1} f_\alpha^0, \tag{31}$$

with coefficients a_i, where $i = 0, 1, 2, \ldots, m-1$. These approximations are elements of the Krylov subspace of dimension m, that is,

$$K^m(A,\ f_\alpha^0) = \text{span}\{f_\alpha^0, Af_\alpha^0, A^2 f_\alpha^0, \ldots, A^{m-1} f_\alpha^0\}, \tag{32}$$

where $A = -\delta t\hat{A}$. The Krylov subspace includes all the polynomial approximations of degree at most $m-1$.

To represent an element of $K^m(A, f_\alpha^0)$ that approximates $f_\alpha^{\tilde{n}}$, one can construct orthonormal sets of vectors $V_m = \{v_1, \ldots, v_m\}$ that are basis of the subspace $K^m(A, f_\alpha^0)$. We take the well-known Arnoldi algorithm [3] to generate the orthonormal basis V_m:

1. Compute $v_1 = f_\alpha^0/\|f_\alpha^0\|$.
2. for $j = 1, \ldots, m$
   (a) $w = Av_j$.
   (b) Do $i = 1, \ldots, j$
      (i) $h_{i,j} = (w, v_i)$
      (ii) $w = w - h_{i,j}v_i$.
   (c) Compute $h_{j+1,j} = \|w\|_2$ and $v_{j+1} = w/h_{j+1,j}$ if $h_{j+1,j} \neq 0$,

which can be summarized as

$$h_{j+1,j}v_{j+1} + \sum_{i=1}^{j} h_{i,j}v_i = Av_j, \quad \text{for each } j = 1, 2, \ldots, m. \tag{33}$$

Relation (33) can be written in a matrix form as

$$V_{m+1}\bar{H} = AV_m, \tag{34}$$

where $\bar{H} = [h_{i,j}] \in R^{(m+1)\times m}$. Defining a Hessenberg matrix $H_m = [h_{i,j}] \in R^{m\times m}$, we have the left-hand side of Eq. (34) as $V_{m+1}\bar{H} = V_m H_m + h_{m+1,m}v_{m+1}e_m^T$, where e_m is the mth unit vector in R^m. Thus we have

$$V_m H_m + h_{m+1,m}v_{m+1}e_m^T = AV_m. \tag{35}$$

When multiplying (35) by V_m^T, we use the fact that V_m is an orthogonal matrix, namely, $V_m^T = V_m^{-1}$, and the Arnoldi vectors v_j are orthonormal so that the second term in the left-hand side of Eq. (35) becomes a null matrix. Thus we obtain

$$H_m = V_m^T A V_m. \tag{36}$$

The Hessenberg matrix, H_m, is the projection of the linear transformation of matrix A onto the Krylov subspace K^m using the orthogonal basis vector V_m. In particular, the best approximation of the exponential in (30) is

$$e^A f_\alpha^0 \approx V_m V_m^T e^A f_\alpha^0 = V_m V_m^T e^A v_1 \|f_\alpha^0\| = \|f_\alpha^0\| V_m V_m^T e^A V_m e_1 \tag{37}$$

$$= \|f_\alpha^0\| V_m e^{H_m} e_1, \tag{38}$$

where $v_1 = f_\alpha^0/\|f_\alpha^0\|$ and $V_m^T v_1 = e_1$.

Friesner et al. [24], and Gallopoulos and Saad [25] have shown that we can obtain an accurate approximation of e^A with small values of m. Also, Saad [3] and Hochbruck and Lubich [26] have conducted a detailed analysis of the error estimate in the Krylov subspace approximation. Novati [27] discussed convergence analysis and efficient timestep-size control technique for time-dependent ODEs, showing that convergence is generally $O(\delta t^{m-1})$ in time.

4. Computational results

In this section, we present convergence analysis of unsteady Couette flow and the computational results for flow over a circular cylinder and flow over two cylinders in tandem.

4.1. Unsteady Couette flow

The test case for the convergence analysis of unsteady Couette flow shows the spatial convergence of the *RK* and the *EXP* schemes for a given time step δt. The computation domain has 6 elements in the vertical direction and a domain size of $[0, L]^2$. The bottom plate is kept stationary while the top plate moves in the x-direction with a velocity U. The periodic

Please cite this article in press as: K.C. Uga, et al., Spectral-element discontinuous Galerkin lattice Boltzmann simulation of flow past two cylinders in tandem with an exponential time integrator, Computers and Mathematics with Applications (2012), doi:10.1016/j.camwa.2011.12.059

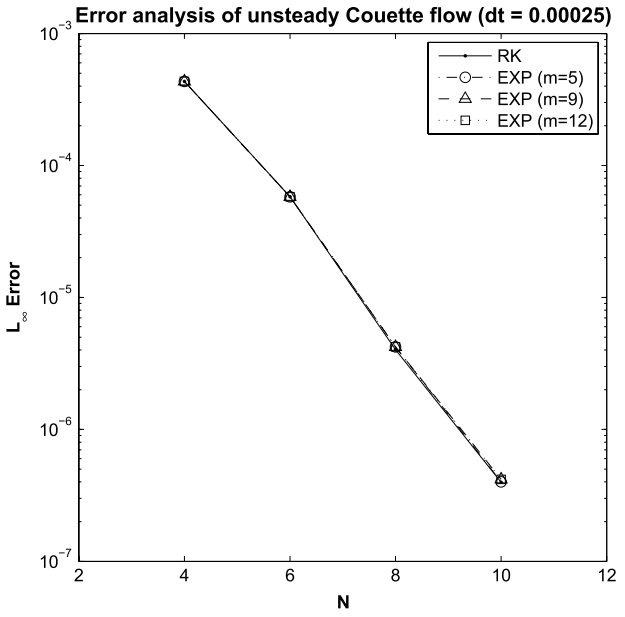

Fig. 2. SEDG-LBM error analysis of unsteady Couette flow at $\delta t = 0.00025$.

boundary condition is applied in the x-direction. The Reynolds number is 2000, Mach Number is 0.05, and the interpolating polynomials considered are $N = 4$, 6, 8 and 10. The exact solution from incompressible Navier–Stokes equations is

$$u(y,t) = U\frac{y}{L} + \sum_{m=1}^{\infty} \frac{2U(-1)^m}{\lambda_m L} e^{-\nu\lambda_m^2 t} \sin(\lambda_m y), \tag{39}$$

for $\lambda_m = \frac{m\pi}{L}$, $m = 1, 2, 3, \ldots$, and $L = 1$. Fig. 2 shows the convergence analysis for $\delta t = 0.00025$ as N is increased. This study was carried out for different orders of Krylov subspace, m, at time $t = 40$. This result shows exponential convergence of both schemes for the weakly imposed bounce back boundary condition [1].

4.2. Flow over a circular cylinder at $Re = 20$

The flow over a circular cylinder is used as a benchmark case to validate the exponential time integration scheme, simply EXP hereafter. The results from this numerical experiment are compared with results from the literature. Several studies of the flow over a circular cylinder have shown that the total drag on the cylinder decreases with increasing Reynolds number [5,28]. Fornberg [28] showed that the drag coefficient on a circular cylinder is about 2.0 for $Re = 20$. He also pointed out that the steady solution for circular cylinder becomes experimentally unsteady for a Reynolds number of about 40. Park et al. [5] showed that with increasing Re, the symmetry in the upstream and downstream disappears and two attached eddies appear behind the cylinder.

We used the EXP scheme to investigate the flow over a circular cylinder at $Re = 20$, Mach number (Ma) at 0.1, and diameter D of the cylinder equal to 1.0. A uniform velocity is imposed at the far-field boundaries. The no-slip boundary condition is imposed on the surface of the cylinder through the flux term as described in [1]. The initial condition is the potential flow solution of the flow over a circular cylinder [29].

Our computational domain has a height of 60D and a width of 70D. The center of the cylinder is placed at a distance of 20D from the inlet boundary as seen in Fig. 3, which shows the mesh on the computational domain that is used for the circular cylinder simulation. The total number of quadrilateral elements in the computational domain is $E = 1118$, with 24 elements on the surface of the cylinder; 16 of the 24 elements are on the rear side of the cylinder. Thus, for a fifth-order spectral element ($N = 5$), we have 144 grid points on the surface of the cylinder. For a given CFL number, the simulation was run until a steady-state solution was reached.

Table 1 shows the drag coefficients C_D and wake length, L, nondimensionalized to the cylinder radius, r_0, of the flow using the five-stage fourth-order Runge–Kutta (RK) scheme [30] and the EXP scheme for different CFL numbers. Table 1 shows that, for a CFL number of 0.25, the drag coefficient and the wake length behind the cylinder are in good agreement for both the RK and EXP schemes. Also, as the CFL number increases, the RK scheme becomes unstable whereas the EXP scheme remains stable.

One of the issues with explicit time-marching schemes such as the RK scheme is the limitations imposed by the CFL number. As the CFL number increases, the scheme becomes unstable. On the other hand, the EXP scheme can handle higher

Please cite this article in press as: K.C. Uga, et al., Spectral-element discontinuous Galerkin lattice Boltzmann simulation of flow past two cylinders in tandem with an exponential time integrator, Computers and Mathematics with Applications (2012), doi:10.1016/j.camwa.2011.12.059

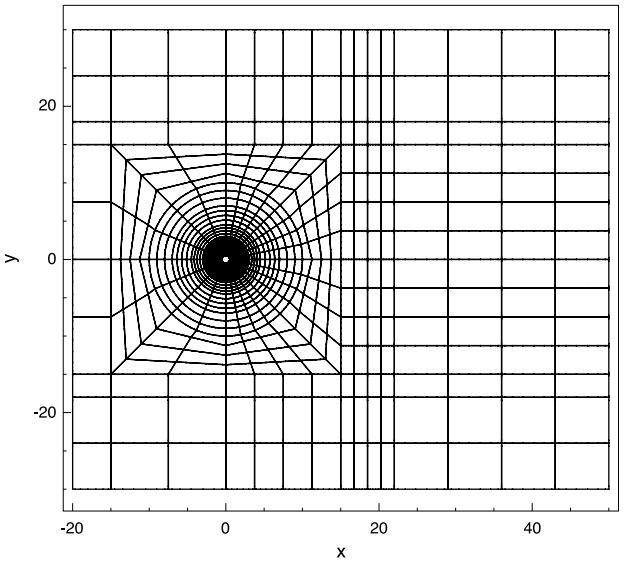

Fig. 3. Mesh and computational domain for a circular cylinder simulation.

Table 1
Drag coefficient and wake length for flow past a single cylinder using RK and EXP schemes with different *CFL* numbers.

CFL	Schemes	C_D	L/r_o
0.25	RK ($N = 7$)	2.102	1.858
0.25	EXP ($m = 9$, $N = 7$)	2.102	1.858
0.50	EXP ($m = 9$, $N = 7$)	2.101	1.861
1.00	EXP ($m = 9$, $N = 7$)	2.099	1.864

Table 2
Comparison of drag coefficient and wake length for $Re = 20$.

Methods	C_D	L/r_o
Lee and Lin (structured mesh) [7]	2.030	1.846
Fornberg [28]	2.000	1.82
Park et al. [5]	2.010	2.000
He and Doolen [6]	2.152	1.842
Niu et al. [8]	2.111	1.92
Dennis and Chang [31]	2.045	1.88
SEDG-LBM (RK, $N = 7$, $CFL = 0.25$, $Ma = 0.1$)	2.102	1.858
SEDG-LBM (EXP, $m = 9$, $N = 7$, $CFL = 0.25$, $Ma = 0.1$)	2.102	1.858
SEDG-LBM (EXP, $m = 9$, $N = 7$, $CFL = 0.50$, $Ma = 0.1$)	2.101	1.861
SEDG-LBM (EXP, $m = 9$, $N = 7$, $CFL = 1.00$, $Ma = 0.1$)	2.099	1.864

CFL numbers as the Krylov subspace dimension increases. The result for *CFL* equal to 1.0 is shown in Table 1. The table shows that as the *CFL* number is increased, there is a slight increase in the wake length. Fig. 4 shows the streamline in the wake region behind the cylinder at $Re = 20$, $Ma = 0.1$, and $CFL = 0.25$. The results in Table 2 show that the drag coefficient and wake length from our simulation are in agreement with the results from the literature.

4.3. Flow over two cylinders in tandem at $Re = 40$

We consider steady flow past two cylinders in tandem for $Re = 40$. The diameters, D, of the cylinders are 1.0, and the spacing between the centers of the two cylinders is $2.5D$. A rectangular computational domain is used in this simulation as seen in Fig. 5. The drag force on the cylinders depends on the Reynolds number and the spacing between the cylinders. At the critical spacing between the cylinders, there is an abrupt increase in the drag coefficient of the upstream and downstream cylinders [10,11]. Also, there is a symmetric vortex exiting behind the rear cylinder, when the spacing between the two cylinder centers is $2.5D$.

The height, H, and width, W, of the computational domain are $60D$ and $20D+s+50D$, respectively, where s is the spacing between the centers of the cylinders. The total number of elements used in the computational domain is $E = 1170$. Thus, for a fifth-order quadrilateral spectral element, the total number of GLL grid points is $n = 42{,}120$. A uniform velocity is

Please cite this article in press as: K.C. Uga, et al., Spectral-element discontinuous Galerkin lattice Boltzmann simulation of flow past two cylinders in tandem with an exponential time integrator, Computers and Mathematics with Applications (2012), doi:10.1016/j.camwa.2011.12.059

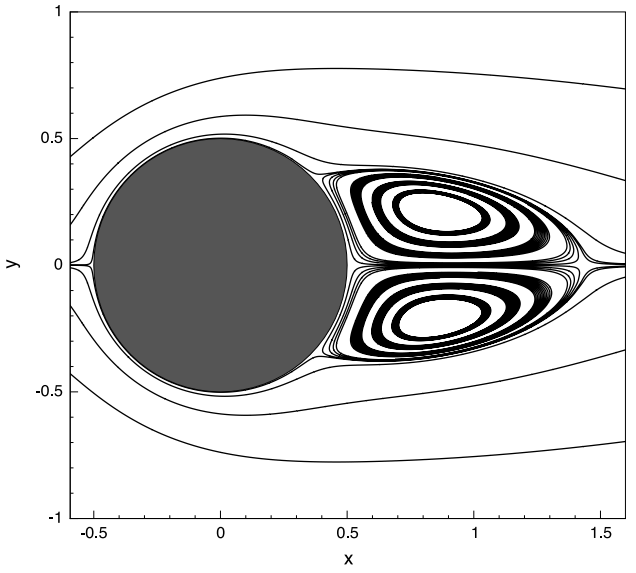

Fig. 4. Streamlines behind a circular cylinder using the EXP scheme, $m = 9$, $N = 7$.

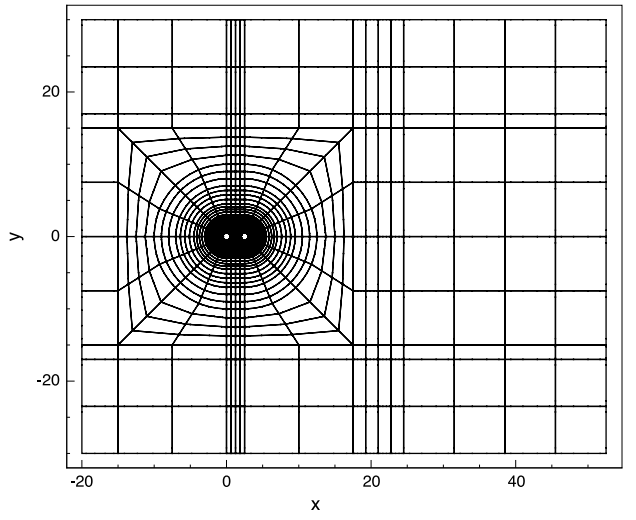

Fig. 5. Computational domain for flow past two circular cylinders in tandem.

imposed at the far-field boundaries, and a no-slip boundary condition based on the bounce-back scheme is imposed on the surface of the cylinders through the flux term [1].

The mesh within the computation domain and a close-up view are shown in Figs. 5 and 6, respectively. The mesh grading is done in such a way that more meshes are put in the region where we have the two cylinders. Farther away from the cylinders we have larger meshes. The aspect ratio of the mesh close to the cylinders is about 5.0. The mesh size increases gradually as we move away from the cylinders, as seen in Fig. 6.

We analyzed the drag coefficient and wake length for the flow past two tandem cylinders using the fourth-order RK scheme and compared these results with the results obtained from the EXP scheme for different element order and Krylov subspace. Table 3 shows the steady-state drag coefficients on the front and rear cylinders for fifth-, seventh-, and ninth-order quadrilateral elements. The table also shows the wake length behind the rear cylinder. The Reynolds number is 40, the Mach number is 0.1, and the *CFL* number is 0.25. Table 3 shows that the drag coefficient on the front cylinder approaches 1.5 as the order of the quadrilateral element increases. This value is the known drag coefficient for an isolated cylinder with the same *Re*. The results also show that the drag coefficient of the rear cylinder approaches 0.062 and the wake length behind the rear cylinder is about 0.93.

Fig. 7 shows the streamlines around the cylinders for a seventh-order quadrilateral element. The wake length is an estimate of the distance between the farthest point on the rear cylinder and the stagnation point behind the rear cylinder. The wake length behind the rear cylinder will change if the spacing between the center of the cylinders is changed. The wake

Please cite this article in press as: K.C. Uga, et al., Spectral-element discontinuous Galerkin lattice Boltzmann simulation of flow past two cylinders in tandem with an exponential time integrator, Computers and Mathematics with Applications (2012), doi:10.1016/j.camwa.2011.12.059

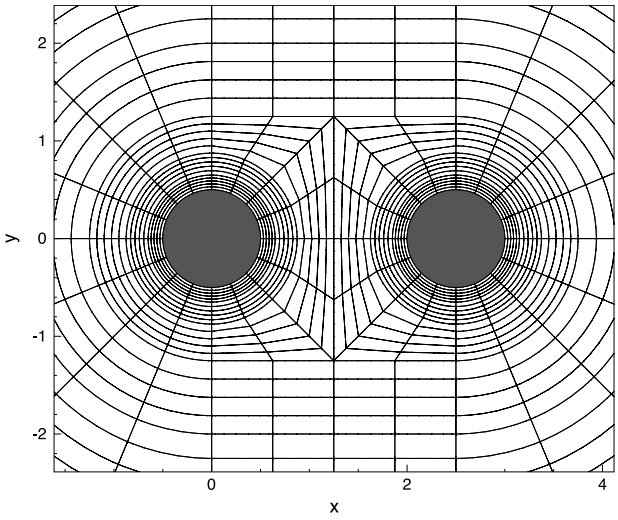

Fig. 6. Close-up view of mesh around two circular cylinders in tandem.

Table 3
Drag coefficient for flow past tandem cylinders using a 5-stage fourth-order RK scheme.

N	C_D (front)	C_D (rear)	L/r_o
5	1.479	0.613×10^{-01}	1.860
7	1.483	0.617×10^{-01}	1.861
9	1.487	0.622×10^{-01}	1.862

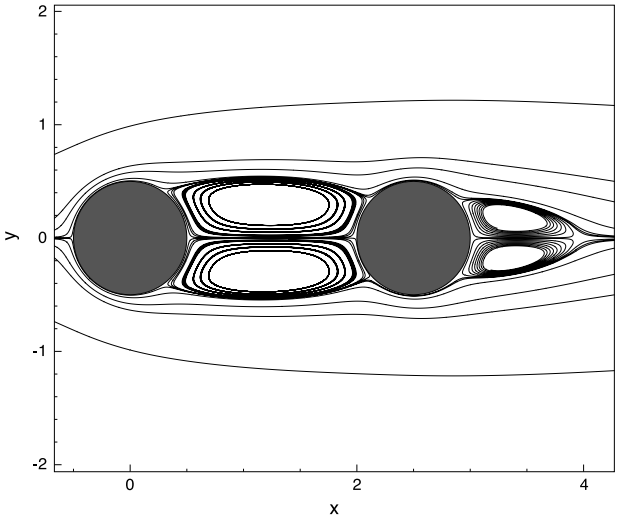

Fig. 7. Streamlines around tandem cylinders for a seventh-order element using the RK scheme.

region behind the front cylinder is not closed because of the presence of the rear cylinder at a location before the zero shear point of an isolated cylinder under the same *Re*. The figure shows that there are two counter-rotating vortices formed behind the front cylinder above and below the centerline. Behind the rear cylinder, the vortices formed are symmetric, closed, and counter-rotating. They are closed because of the adequate spacing behind the rear cylinder, which allows for a zero shear point to exist. The pressure distribution around the cylinders for a seventh-order element is shown in Fig. 8. The results show that the low drag coefficient on the rear cylinder is caused by the low-pressure region between the two cylinders and the downstream region. The vortices between the rear of the first cylinder and the front of the rear cylinder create a pulling effect on the faces of the cylinder in this region as they rotate in opposite direction. The front cylinder experiences a positive pressure on the front side and a negative pressure on the rear side. Thus it experiences a large drag force because of the low-pressure region on the rear side.

Please cite this article in press as: K.C. Uga, et al., Spectral-element discontinuous Galerkin lattice Boltzmann simulation of flow past two cylinders in tandem with an exponential time integrator, Computers and Mathematics with Applications (2012), doi:10.1016/j.camwa.2011.12.059

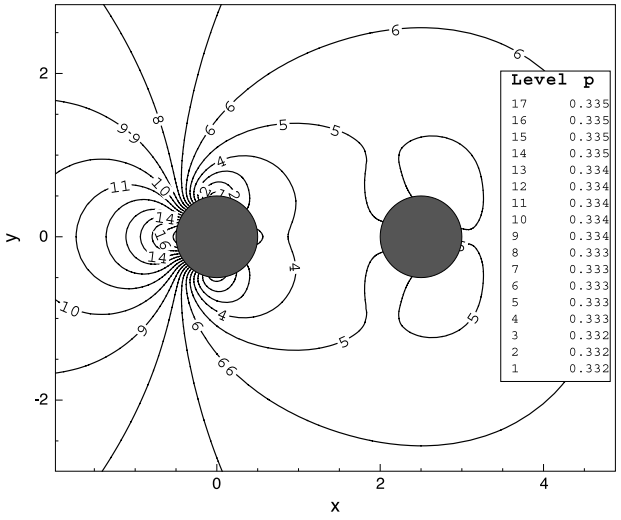

Fig. 8. Pressure contour around tandem cylinders for a seventh-order element using the RK scheme.

Table 4
Drag coefficients for flow over tandem cylinders using the EXP scheme, $CFL = 0.25$.

m	N	C_D (front)	C_D (rear)	L/r_o
	5	1.479	0.613×10^{-01}	1.858
5	7	1.483	0.617×10^{-01}	1.860
	9	1.487	0.622×10^{-01}	1.862
7	5	1.479	0.613×10^{-01}	1.860
	7	1.483	0.617×10^{-01}	1.858
9	5	1.479	0.613×10^{-01}	1.860
	7	1.483	0.617×10^{-01}	1.862

Table 5
Drag coefficients for flow over tandem cylinders using the EXP scheme, $CFL = 2$.

m	N	C_D (front)	C_D (rear)	L/r_o
7	7	1.474	0.537×10^{-01}	2.131
7	9	1.483	0.591×10^{-01}	1.977
9	7	1.475	0.613×10^{-01}	1.868
9	9	1.482	0.619×10^{-01}	1.865
11	7	1.476	0.614×10^{-01}	1.862
11	9	1.482	0.620×10^{-01}	1.861

For the same *Re*, *Ma*, *CFL* numbers, and element order, the simulations were carried out by using the EXP scheme with $m = 5$, 7, and 9. Table 4 shows the results from the simulations with the EXP scheme. It shows that for a given order of the Krylov subspace m, as the order of the quadrilateral element N increases, the drag coefficient for the front cylinder approaches 1.5, and the drag coefficient of the rear cylinder approaches 0.062. This is the same behavior that was seen with the RK scheme. For this *CFL* number, we note that even for a small m, we can get an accurate estimate of the drag coefficients. The streamlines around the cylinders for $m = 5$ and $N = 5$ are shown in Fig. 9. The pressure contour around the cylinders for $m = 5$ and $N = 5$ is shown in Fig. 10.

Simulations for $CFL = 2$ were carried out for the same *Re* and *Ma*; the results are shown in Table 5. A comparison of the results from the EXP scheme with varying *CFL* number and m is shown in Table 6. The results from Table 6 show that even for high *CFL* numbers, the drag results from the EXP scheme are consistent with the results from the RK scheme as seen in Table 3. Table 6 also shows that by increasing m and N, we can get a better estimate of the drag coefficients on the cylinders. This is in agreement with the discussion in the earlier section. Table 7 presents a comparison of flow parameters between our solution and those of Singha and sinhamahapatra [12] for $Re = 40$. Our result shows good agreement for the drag coefficient on the front cylinder.

Please cite this article in press as: K.C. Uga, et al., Spectral-element discontinuous Galerkin lattice Boltzmann simulation of flow past two cylinders in tandem with an exponential time integrator, Computers and Mathematics with Applications (2012), doi:10.1016/j.camwa.2011.12.059

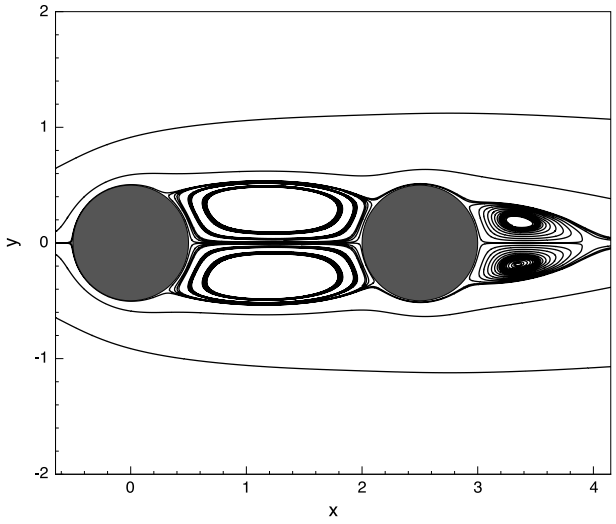

Fig. 9. Streamlines around tandem cylinders for a fifth-order element using the EXP scheme.

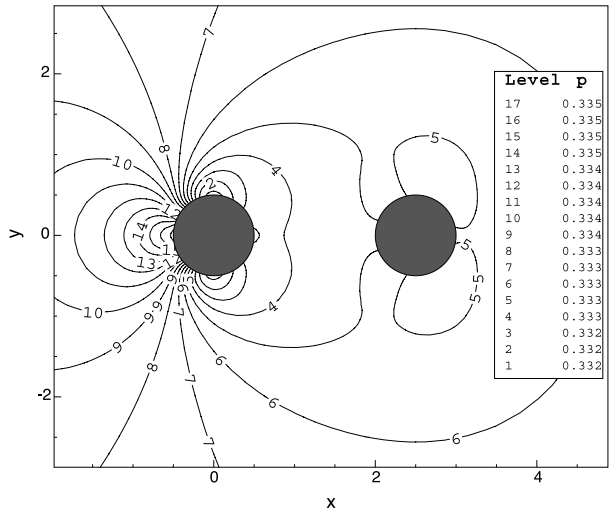

Fig. 10. Pressure contour around tandem cylinder for a fifth-order element using the EXP scheme.

Table 6
Comparison of drag coefficient and wake length for flow past tandem cylinders using the EXP scheme.

N	CFL	m	C_D (front)	C_D (rear)	L/r_o
7	0.25	7	1.483	0.617×10^{-01}	1.858
7	0.50	7	1.483	0.617×10^{-01}	1.862
7	1.00	7	1.482	0.616×10^{-01}	1.861
7	2.00	7	1.474	0.537×10^{-01}	2.131
7	0.25	9	1.483	0.617×10^{-01}	1.862
7	0.50	9	1.483	0.617×10^{-01}	1.856
7	1.00	9	1.482	0.616×10^{-01}	1.861
7	2.00	9	1.475	0.613×10^{-01}	1.868

5. Conclusions

We have presented an exponential time integrator scheme for spectral-element discontinuous Galerkin lattice Boltzmann simulations of flow past a circular cylinder and tandem cylinders. The computational results in the case for flow over a circular cylinder are in agreement with the results from the literature as presented in Section 4.2.

Please cite this article in press as: K.C. Uga, et al., Spectral-element discontinuous Galerkin lattice Boltzmann simulation of flow past two cylinders in tandem with an exponential time integrator, Computers and Mathematics with Applications (2012), doi:10.1016/j.camwa.2011.12.059

Table 7
Comparison of drag coefficients and wake length for flow past tandem cylinders, $s = 2.5D$, $CFL = 0.25$, $N = 7$, and $m = 9$.

	RK	EXP	Singha et al. [12]
C_D (front)	1.483	1.483	1.49
C_D (rear)	0.617×10^{-01}	0.617×10^{-01}	0.18
L/r_o	1.861	1.862	–

For the flow past two tandem circular cylinders, we have shown that for a *CFL* number of 0.25 and Reynolds number of 40, the accuracy of the approximated results increases with increasing quadrilateral element order and the order of the Krylov subspace. This conclusion can also be drawn from the fact that the matrix exponential is accurate when the order of the Krylov subspace is equal to the size of the large matrix *A*. Thus, approximation accuracy increases with increasing order of Krylov subspace. Also, the tabulated results for tandem cylinders using the exponential scheme show that the approximated results for drag coefficient and wake length are correct even for large *CFL* numbers.

Acknowledgments

This work was partially supported by the Office of Advanced Scientific Computing Research, Office of Science, US. Department of Energy, under Contract DE-AC02-06CH11357, while KCU worked as a summer intern at the Mathematics and Computer Science Division at Argonne National Laboratory. TL was supported by the National Science Foundation grant DMS-0811046 and Nuclear Regulatory Commission grant NRC-38-09-947. KCU also appreciates the travel support from NSF to attend ICMMES-2010.

References

[1] M. Min, T. Lee, A spectral-element discontinuous Galerkin lattice-Boltzmann method for incompressible flows, J. Comput. Phys. 230 (2011) 245–259.
[2] M. Min, P.F. Fischer, An efficient high-order time integration method based on Krylov approximations, Preprint ANL/MCS-P1830-0111, 2011.
[3] Y. Saad, Analysis of some Krylov subspace approximations to the matrix exponential operator, SIAM J. Numer. Anal. 29 (1992) 209–228.
[4] E. Gallopoulos, Y. Saad, Efficient solution of parobolic equations by Krylov approximation methods, SIAM J. Sci. Stat. Comput. 13 (1992) 1236–1264.
[5] J. Park, K. Kwon, H. Choi, Numerical solutions of flow past a circular cylinder at Reynolds number up to 160, KSME Int. J. 12 (1998) 1200–1205.
[6] X. He, G. Doolen, Lattice Boltzmann method on curvilinear coordinate systems: flow around a circular cylinder, J. Comput. Phys. 134 (1997) 306–315.
[7] T. Lee, C.-L. Lin, A characteristic Galerkin method for discrete Boltzmann equation, J. Comput. Phys. 171 (2001) 336–356.
[8] X.D. Niu, Y.T. Chew, C. Shu, Simulation of flows around an impulsively started circular cylinder by Taylor series expansion-and least square-based lattice Boltzmann method, J. Comput. Phys. 188 (2003) 176–193.
[9] M.M. Zdravkovich, Flow Around Circular Cylinders—Volume 1: Fundamentals, Oxford University Press, Oxford, 1997.
[10] B. Sharman, F.S. Lien, L. Davidson, C. Norberg, Numerical predictions of low Reynolds number flows over two tandem circular cylinders, Internat. J. Numer. Methods Fluids 47 (2005) 423–447.
[11] A. Mussa, P. Asinari, L.-S. Luo, Lattice Boltzmann simulations of 2D laminar flows past two tandem cylinders, J. Comput. Phys. 228 (2009) 983–999.
[12] S. Singha, K.P. Sinhamahapatra, High-resolution numerical simulation of low Reynolds number incompressible flow about two cylinders in tandem, J. Fluids Eng. 132 (2010) 011101.
[13] M.O. Deville, P.F. Fischer, E.H. Mund, High-Order Methods for Incompressible Fluid Flow, in: Cambridge Monographs on Applied and Computational Mathematics, Cambridge University Press, 2002.
[14] P.L. Bhatnagar, E.P. Gross, M. Krook, A model for collision processes in gases, I: small amplitude processes in charged and neutral one-component system, Phys. Rev. 94 (1954) 511–525.
[15] D.A. Wolf-Gladrow, Lattice-Gas Cellular Automata and Lattice Boltzmann Models: An Introduction, Springer, Berlin, 2005.
[16] S. Succi, The Lattice Boltzmann Equation: For Fluid Dynamics and Beyond, Oxford University Press, 2001.
[17] Y.H. Qian, D. D'Humières, P. Lallemand, Lattice BGK models for Navier–Stokes equation, Europhys. Lett. 17 (1992) 479–484.
[18] X. He, S. Chen, G.D. Doolen, A novel thermal model for the lattice Boltzmann method in incompressible limit, J. Comput. Phys. 146 (1998) 282–300.
[19] J.S. Hesthaven, T. Warburton, Nodal Discontinuous Galerkin Methods, Algorithms, Analysis, and Applications, in: Texts in Applied Mathematics, Springer, 2008.
[20] F.X. Giraldo, M. Restelli, A study of spectral element and discontinuous Galerkin methods for the Navier–Stokes equations in nonhydrostatic atmospheric modelling: equation set and test cases, J. Comput. Phys. 227 (2008) 3849–3877.
[21] F.X. Giraldo, T. Warburton, A triangular discontinuous Galerkin oceanic shallow water model, Internat. J. Numer. Methods Fluids 56 (2008) 899–925.
[22] C. Pozrikidis, Introduction to Finite and Spectral Element Methods using MATLAB, Chapman and Hall, CRC, 2005.
[23] M. Min, J. Fu, T. Lee, Parallel performance for the spectral-element discontinuous Galerkin lattice Boltzmann method for incompressible flows, Preprint ANL/MCS-P1831-1010, 2011.
[24] R.A. Friesner, L.S. Tuckerman, B.C. Dornblaser, T.V. Russo, A method for exponential propagation of large systems of stiff nonlinear differential equations, J. Sci. Comput. 4 (1989) 327–354.
[25] E. Gallopoulos, Y. Saad, Parallel solution of parabolic equations using polynomial approximation to the exponential, research institute for advanced computer science, Tech. Report 90-14, SIAM J. Sci. Stat. Comput., vol. 13, 1992.
[26] M. Hockbruck, C. Lubich, On Krylov subspace approximation to the matrix exponential operator, SIAM J. Numer. Anal. 34 (1997) 1911–1925.
[27] Novati Paolo, A low cost Arnoldi method for large linear initial value problems, Int. J. Comput. Math. 81 (7) (2004) 835–844.
[28] B. Fornberg, A numerical study of steady viscous flow past a circular cylinder, J. Fluid Mech. 98 (1980) 819–855.
[29] G.K. Batchelor, An Introduction to Fluid Dynamics, Cambridge University Press, 1967.
[30] M.H. Carpenter, C. Kennedy, Fourth-order 2N-storage Runge–Kutta schemes, NASA Report TM 109112, NASA Langley Research Center, 1994.
[31] S.C.R. Dennis, G.Z. Chang, Numerical solutions for flow past a circular cylinder at Reynolds number up to 100, J. Fluid Mech. 42 (1970) 471–481.

Please cite this article in press as: K.C. Uga, et al., Spectral-element discontinuous Galerkin lattice Boltzmann simulation of flow past two cylinders in tandem with an exponential time integrator, Computers and Mathematics with Applications (2012), doi:10.1016/j.camwa.2011.12.059